Proceedings of the 29th Annual International
Conference of the IEEE EMBS
Cité Internationale, Lyon, France
August 23-26, 2007.

Parameter Identification for a Needle-Tissue Interaction Model

Ehsan Dehghan, Xu Wen, Reza Zahiri-Azar, Maud Marchal and Septimiu E. Salcudean

Abstract— **In this work, needle-tissue interaction forces are modeled by a three parameter force distribution composed of two step functions with variable amplitudes and spacing. A finite element based simulation is used to adjust the parameters and fit the simulation results to the experimental data. In experiments, needle displacements and needle base forces were measured along with tissue displacements. A real-time version of the time-domain cross-correlation method was employed in this study to estimate the tissue displacements from ultrasound radio-frequency data, as done in elastography. In addition to the force model parameters, the elastic parameters of the tissue were adjusted to match the simulated and measured displacements.**

I. Introduction

Accurate placement of the needle is still a challenge in medical treatments involving needle insertion into soft deformable tissues. As an example, during a prostate brachytherapy procedure, several radioactive capsules are implanted inside the prostate and surrounding tissue using a long needle with visual guidance from trans-rectal ultrasound (TRUS) and real-time X-ray fluoroscopy. Prostate deformation and rotation during the needle penetration [1] can lead to targeting errors [2] which in turn can result in under-dosed and over-dosed regions and subsequent complications. Significant skill is required to compensate for tissue deformations and decrease the targeting errors. Thus, brachytherapy simulators [3], [4] and path planners can be helpful for physician training purposes, pre-operative planning and robotic surgery.

In order to simulate the needle insertion process, it is necessary to have a model for needle-tissue interactions. There has been extensive research on this topic [5]–[9]. Okamura *et al.* [5] inserted a needle into a bovine liver and divided the forces applied by the tissue to the needle into three parts: 1) capsule stiffness; 2) friction and 3) cutting forces occurring at the needle tip. This model was derived from measured forces at the needle base without tracking the tissue displacements. Podder *et al.* [6] developed a patient-specific and procedure-specific statistical model to estimate the maximum needle force during insertion into the prostate and the perineum. The forces were measured during brachytherapy for 25 patients. DiMaio and Salcudean [7] identified a two-parameter force profile along the needle – a peak at the tip, following a constant shaft force density – by measuring the insertion force during penetration of a needle into a slab of PVC. To derive the model, they also measured the tissue motion by tracking the position of superficial markers using a camera. Hing *et al.* [8] tracked the displacements of several implanted fiducial beads during needle insertion using a dual C-arm fluoroscope setup. They identified a local effective modulus during puncture and an approximate cutting force for soft tissue samples. Crouch *et al.* [9] inserted a needle into a transparent and homogeneous silicon gel phantom in which several layers of fiducial markers were implanted. They tracked the marker displacements in 3-D using two digital cameras and introduced a velocity-dependent needle shaft force density – a constant shaft force density following a peak and a dip at the needle tip.

In this work, a force model for needle-tissue interaction is derived based on the tissue displacement estimates and the insertion force recorded during an experiment. A three parameter force distribution along the needle was chosen, inspired by the shape of the recorded force. The three parameters of the force model and the Young's modulus are the parameters to be identified for each part of the tissue. The force model is validated using the experimental data recorded during insertion of a needle into phantom as reported in [10]. Needle base position, forces and tissue displacements were measured during the experiment. A finite element simulation was used to adjust the parameters and match the simulated and measured data.

This paper is organized as follows. In Sec. II the needle-tissue interaction model is presented, followed by the identification method. The experiment setup, the ultrasound based displacement tracking method, measured data and modeling results are presented in Sec. III. Conclusions are drawn in Sec. IV.

II. Needle Shaft Force Density

The force density on the needle shaft during the insertion phase is modeled using two superimposed step functions with variable amplitude and spacing – as shown in Fig. 1(a). The model is inspired by the shape of the measured force during the insertion of the needle as illustrated in Fig. 3(b). The needle base force shows a higher slope when the needle starts to penetrate into a new part of tissue. This high slope increase is followed by a more gradual increase when the needle is well advanced into the tissue. For example, see parts 1 and 3 as opposed to parts 2 and 4 in Fig. 3(b), showing the force feedback during penetration of the needle into a phantom with a harder inclusion. The three parameters of the needle force distribution that need to be identified are:

S.E. Salcudean (corresponding author), E. Dehghan, X. Wen and R. Zahiri-Azar are with the Department of Electrical and Computer Engineering, University of British Columbia, Vancouver, BC, Canada. {tims, ehsand,wenx,zahiri}@ece.ubc.ca

M. Marchal was with TIMC-GMCAO Laboratory, Grenoble, France. She is now with the department of Electrical and Computer Engineering, University of British Columbia, Vancouver, BC, Canada. maudm@ece.ubc.ca

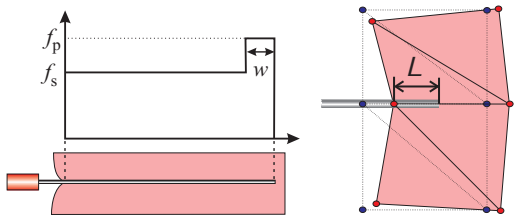

Fig. 1. (a) The needle shaft force density, and (b) The length L over which the force is integrated in the deformed configuration. The dotted lines show the elements in the undeformed configuration.

(i) f_s, the amplitude of the constant shaft force density that simulates friction, (ii) f_p, the amplitude of the peak force density near the needle tip that simulates cutting forces, and (iii) the width w of the peak force density. For parameter identification, the needle insertion was simulated using a linear FEM based model. The force profile shown in Fig. 1(a) was implemented in the simulator and the corresponding displacements for nodes were simulated. The force density was integrated on the part of the needle which was inside the tissue in the deformed configuration. This length is shown as L in Fig. 1(b). Due to tissue deformation, this length is unknown. Therefore, an iterative method was used to find the equilibrium point. At this point, the force is distributed on the tissue mesh nodes which are in contact with the needle, according to their relative position in the deformed configuration. This force is applied as a force boundary condition in the axial direction. Two displacement boundary conditions are applied in the other directions to keep the nodes sliding along the needle. To achieve higher accuracy, the mesh adaptation algorithm [4] was used. In this algorithm, every time the needle tip arrives at a new element boundary, the closest element node is re-positioned on the needle tip in the reference mesh.

The elastic parameters of the tissue – Young's modulus (E) and Poisson's ratio (ν) – were not known. To solve this problem, a Poisson's ratio was assumed for the tissue prior to the simulation. The three parameters for the force profile and the Young's modulus of each part of the tissue were identified from the comparison of the measured and the simulated data using the following algorithm:

1) Assign a set of Young's modulus and force density parameters to each part of the tissue.
2) Simulate the insertion with the given parameters and find the simulated needle base force and the axial displacement of the nodes.
3) Update the force density parameters. The parameter w for each part of the tissue can be updated using the difference between the width of the high slope part of the simulated and the measured force (i.e. parts 1 and 3 in Fig. 3(b)). Parameters f_p and f_s for each tissue type can be updated using the difference between the average slope of the measured and simulated base forces in the corresponding time portions (i.e. average slope of parts 1 and 3 for f_ps and slope of parts 2 and 4 for f_ss).
4) Goto 2 unless the error between the simulated and measured base forces is small.
5) Compare the measured and simulated average axial displacements of nodes and update the Young's moduli to decrease the error. Repeat from 2 until a convergence criterion is met.

Due to mismatch between the FEM model and the real tissue, it is impossible to find a perfect fit between nodal displacements. Therefore, the iterations are continued until the changes in the elastic parameters do not decrease the error. Please note that the lateral displacement was assumed to be negligible compared to the axial displacements.

III. Experimental Results

To acquire experimental data, the following experiment was performed on a phantom.

A. Experiment Setup

In the experiment, an 18 gauge brachytherapy needle (Bard, NJ, USA) was inserted into a specially designed non-homogeneous phantom composed of a harder inclusion surrounded by a softer tissue. The harder inclusion – designed to mimic the prostate – was made from 100% polyvinyl chloride (PVC) plasticizer (M-F Manufacturing Co., Inc. Fort Worth, TX, USA), while the outside substrate was made from 66.7% PVC plasticizer and 33.3% plastic softener (M-F Manufacturing Co., Inc. Fort Worth). The inclusion was connected to the base with a cylinder of the same material. Cellulose (Sigma-Aldrich Inc., St. Louis, MO, USA) was added to the two parts as scattering particles. A cylindrical hole through the phantom represents the rectum. A stiff cylinder was inserted into this hole to simulate the rectal probe which is used during brachytherapy. During the FEM based simulation, the nodes in contact with this cylinder and the nodes located at the back and bottom of the phantom, were assumed to be fixed. Figure 2(b) shows the schematic diagram of the phantom. To control the insertion speed, the needle was mounted on a translational lead-screw stage powered by a heavily geared Maxon DC motor with an optical encoder (see Fig. 2(a)). The speed of the drive motor was adjusted by a proportional controller. A computer was used to implement the controller and to record the insertion and retraction forces measured by a load cell (MBD-2.5 Transducer Techniques, CA, USA) mounted at the base of the needle. The sampling frequency for force measurements was 20 Hz.

B. Ultrasound Based Deformation Tracking

A Sonix RP PC-based ultrasound machine and an L12-5 38-mm linear probe (Ultrasonix Medical Corp. Burnaby, BC, Canada) were used in our experiments. The phantom was imaged to a depth of 75 mm using a linear array of 128 elements with 1.6 lines per millimeter in the lateral direction (70% sector). The centroid frequency was 5 MHz. Both B-mode images and RF frames were captured at 20 frames per second synchronized with the computer which controlled the

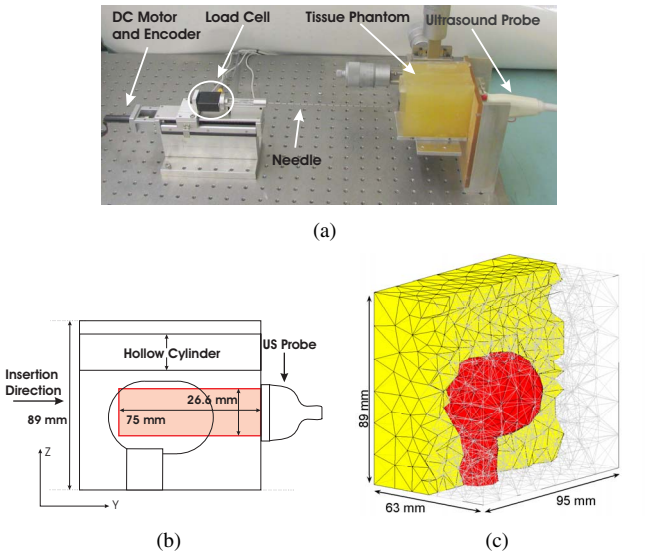

Fig. 2. (a) The experiment setup, (b) Side view of the phantom, showing the inclusion, hollow cylinder and the US field of view, and (c) Tissue phantom meshed with tetrahedral elements.

insertion device and recorded the force data. The position of the ultrasound probe with respect to the tissue and the US field of view inside the tissue are shown in Fig. 2(b).

The Time-Domain Cross-Correlation with Prior Estimates (TDPE) was used to process the data off-line and estimate the axial component of the displacement [11] (along y axis as shown in Fig. 2(b)). Each RF-line was divided into 120 overlapping windows (1 mm window length and 60% window overlap). In this method, absolute motions are estimated by integration of relative motions. To increase the accuracy of the estimation, a dynamic reference frame updating algorithm was used in which the reference frame is updated every time the correlation between the current frame and the reference frame drops below a threshold [10]. At each step, the absolute displacements for every spatial location were reported as the estimated motions at that location added to the accumulated displacement values in the integrator.

C. Force and Displacement Measurements

The needle was inserted and retracted along the y axis according to the controlled position shown in Fig. 3(a). The insertion line was 5 mm out of the US field of view to avoid the deteriorating effects of a metallic object on the US images and to increase the accuracy of the tracking algorithm.

To be employed in the FEM simulator, the tissue phantom was meshed using 991 nodes and 4453 linear tetrahedral elements as shown in Fig. 2(c). The axial displacement of the mesh nodes located in the US field of view were measured during the experiment and are shown in Fig. 3(c). This figure shows non-zero measured nodal displacements after the needle was fully retracted. This drift is due to the accumulation of residuals caused by integration of relative motions. The measured force is shown in Fig. 3(b). The decrease in the force when the needle stops is due to

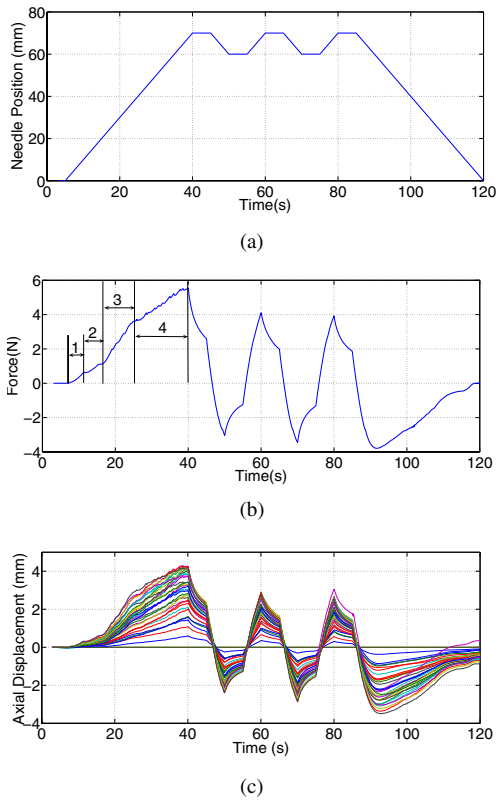

Fig. 3. (a) Needle tip position vs. time, (b) Measured insertion force, (c) Axial displacements of the nodes located on the US plane. The needle was partially retracted and inserted again after the main insertion. Since in the second and third insertions, the needle was inserted in the same path as the first insertion, no cutting happened. Therefore, the second and third peak forces (t=60 and 80 s) are smaller than the first one (t =40 s).

TABLE I

NEEDLE SHAFT FORCE DENSITY AND ELASTIC PARAMETERS

ν	Tissue	f_s(N/m)	f_p(N/m)	w(mm)	E(kPa)
0.45	Inclusion	70	400	5.7	14
	Surrounding	60	180	3.0	9.5
0.49	Inclusion	72	320	7.0	10
	Surrounding	60	140	4.0	7.0

relaxation of viscoelastic tissue.

The force model parameters and the Young's modulus for each part of the tissue were adjusted to model the measured needle force during the main insertion part ($0 \leq t \leq 40$ s), thus tissue relaxation is not simulated. The displacement drift was assumed to be negligible during this time. Due to slow speed of insertion, the FEM simulation was performed in quasi-static mode. The parameter identification was performed with two choices for the Poisson's ratio. At first the Poisson's ratio was assumed to be 0.45 for both the inclusion and the surrounding tissue. In another case, the Poisson's ratio was assumed to be 0.49 to simulate near incompressibility. The identified force density and material elastic parameters are shown in Table I for the given phantom and different Poisson's ratios. The simulated and measured forces are shown in Fig. 4(a). The maximum error between simulated and measured forces is 0.33 N for $\nu = 0.49$ and 0.38 N

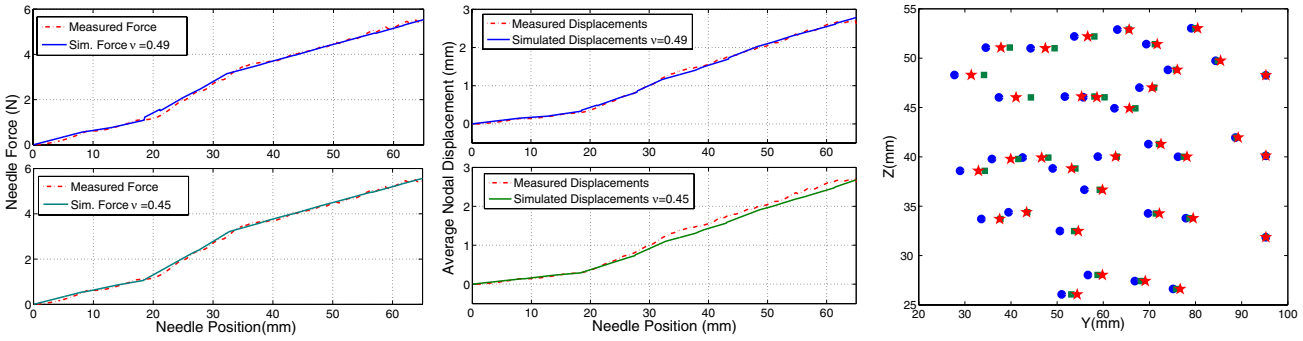

(a) (b) (c)

Fig. 4. (a) Simulated and measured insertion forces, (b) Simulated and measured average of nodal displacements in the axial direction, and (c) Position of the nodes in the US field of view; (circles) the original position, (squares) simulated positions and (stars) positions measured with TDPE. Only axial displacements were applied.

for $\nu = 0.45$. Figure 4(a) shows the ability of the proposed force density to simulate the measured needle force with high accuracy. Figure 4(b) details the average simulated and measured axial displacements for the nodes on the ultrasound field of view. The simulated axial displacement has a maximum average error of 0.1 mm and standard deviation of 1.2 mm for $\nu = 0.49$ and maximum average error of 0.4 mm and standard deviation of 1.9 mm for $\nu = 0.45$. Figure 4(c) shows the position of the nodes in the US field of view in the deformed and undeformed configurations. Only axial displacements are represented in this figure and the Poisson's ratio is 0.49. It can be seen that when the parameters are identified with $\nu = 0.49$, the model can predict tissue deformation with higher accuracy. There is a sudden change in the simulated force in Fig. 4(a) when the Poisson's ratio is 0.49 (t=18.4 s and t=21.6 s). This sudden change is due to the topological changes caused by the mesh adaptation algorithm. In contrast, the simulated force with ν=0.45 does not change suddenly. Lower Poisson's ratios tend to react more smoothly to this topological change.

IV. Conclusion and Future Work

In this paper, a model of the interactions between soft tissues and a needle has been presented by using a new experimental approach based on ultrasound imaging. The model was fitted to the measured force-displacement data acquired from insertion of a brachytherapy needle into a non-homogeneous PVC phantom. The displacements were estimated from RF data using an ultrasound based method. No fiducial beads were implanted and the transparency of the material was not necessary. A record of the applied forces on the needle base was used to find the values of a three-parameter needle shaft force density. The Young's moduli of the tissues were adjusted to fit the simulated axial displacements to the measured axial displacements. Finite element simulations were used to adjust the unknown parameters. The proposed force profile and the identified elastic properties can be used to construct an FEM simulator to simulate the needle insertion process for path planning and for physician training.

In the future, the needle insertion experiment will be performed with different insertion speeds to investigate the velocity dependent properties of the force profile. Statistical analysis will be carried out by acquiring more insertion data from the phantom. In this work, the major displacements were in the axial direction of the US image. However, during brachytherapy, the needle motion and major tissue displacements are in the lateral direction of the sagittal/para-sagittal US image acquired using the trans-rectal probe. Estimation of the lateral motion with higher accuracy will be the subject of further research.

References

[1] V. Lagerburg, M. Moerland, J. Lagendijk, and J. Battermann, "Measurement of prostate rotation during insertion of needles for brachytherapy," *Radiotherapy and Oncology*, vol. 77, pp. 318–323, 2005.

[2] R. Teschereau, J. Pouliot, J. Roy, and D. Tremblay, "Seed misplacement and stabilizing needles in transperineal permanent prostate implants," *Radiotherapy and Oncology*, vol. 55, pp. 59–63, 2000.

[3] R. Alterovitz, J. Pouliot, R. Taschereau, I. C. Hsu, and K. Goldberg, "Needle insertion and radioactive seed implantation in human tissue: Simulation and sensitivity analysis," in *Proc. IEEE ICRA*, 2003, pp. 1793–1799.

[4] O. Goksel, S. E. Salcudean, and S. P. DiMaio, "3D simulation of needle-tissue interaction with application to prostate brachytherapy," *Computer Aided Surgery*, vol. 11, no. 6, pp. 279–288, 2006.

[5] A. Okamura, C. Simone, and M. O'Leary, "Force modeling for needle insertion into soft tissue," *IEEE Trans. Biomed. Eng.*, vol. 51, pp. 1707 – 1716, 2004.

[6] T. Podder, J. Sherman, E. Messing, D. Rubens, D. Fuller, J. Strang, R. Brasacchio, and Y. Yu, "Needle insertion force estimation model using procedure-specific and patient-specific criteria," in *Proc. IEEE EMBS Int. Conf.*, 2006, pp. 555–558.

[7] S. P. DiMaio and S. E. Salcudean, "Needle insertion modeling and simulation," *IEEE Trans. Robot. and Autom.*, vol. 19, pp. 864 – 875, 2003.

[8] J. T. Hing, A. D. Brokks, and J. P. Desai, "A biplanar fluoroscopic approach for the measurement, modeling, and simulation of needle and soft-tissue interaction," *Medical Image Analysis*, vol. 11, pp. 62–78, 2007.

[9] J. R. Crouch, C. M. Schneider, J. Wainer, and A. M. Okamura, "A velocity-dependent model for needle insertion in soft tissue," in *Proc. MICCAI*, 2005, pp. 624–632.

[10] E. Dehghan, X. Wen, R. Zahiri-Azar, M. Marchal, and S. E. Salcudean, "Modeling of needle-tissue interaction using ultrasound-based motion estimation," in *Proc. MICCAI*, 2007.

[11] R. Zahiri-Azar and S. E. Salcudean, "Motion estimation in ultrasound images using time domain cross correlation with prior estimates," *IEEE Trans. Biomed. Eng.*, vol. 53, pp. 1990–2000, 2006.